BIOCHEMISTRY
including biophysical chemistry & molecular biology

Article

pubs.acs.org/biochemistry

The Lack of Synchronization between Iron Uptake and Cell Growth Leads to Iron Overload in *Saccharomyces cerevisiae* during Post-exponential Growth Modes

Jinkyu Park,[†] Sean P. McCormick,[†] Mrinmoy Chakrabarti,[†] and Paul A. Lindahl*[,†,‡]

[†]Department of Chemistry, Texas A&M University, College Station, Texas 77843-3255, United States
[‡]Department of Biochemistry and Biophysics, Texas A&M University, College Station, Texas 77843-2128, United States

S *Supporting Information*

ABSTRACT: Fermenting cells growing exponentially on rich (YPAD) medium underwent a transition to a slow-growing state as glucose levels declined and their metabolism shifted to respiration. During exponential growth, Fe import and cell-growth rates were matched, affording an approximately invariant cellular Fe concentration. During the transition period, the high-affinity Fe import rate declined slower than the cell-growth rate declined, causing Fe to accumulate, initially as Fe^{III} oxyhydroxide nanoparticles but eventually as mitochondrial and vacuolar Fe. Once the cells had reached slow-growth mode, Fe import and cell-growth rates were again matched, and the cellular Fe concentration was again approximately invariant. Fermenting cells grown on minimal medium (MM) grew more slowly during the exponential phase and underwent a transition to a true stationary state as glucose levels declined. The Fe concentration of MM cells that just entered the stationary state was similar to that of YPAD cells, but MM cells continued to accumulate Fe in the stationary state. Fe initially accumulated as nanoparticles and high-spin Fe^{II} species, but vacuolar Fe^{III} also eventually accumulated. Surprisingly, Fe-packed 5-day-old MM cells suffered no more reactive oxygen species (ROS) damage than younger cells, suggesting that the Fe concentration alone does not accurately predict the extent of ROS damage. The mode and rate of growth at the time of harvesting dramatically affected cellular Fe content. A mathematical model of Fe metabolism in a growing cell was developed. The model included the import of Fe via a regulated high-affinity pathway and an unregulated low-affinity pathway. The import of Fe from the cytosol to vacuoles and mitochondria and nanoparticle formation were also included. The model captured essential trafficking behavior, demonstrating that cells regulate Fe import in accordance with their overall growth rate and that they misregulate Fe import when nanoparticles accumulate. The lack of regulation of Fe in yeast is perhaps unique compared to the tight regulation of other cellular metabolites. This phenomenon likely derives from the unique chemistry associated with Fe nanoparticle formation.

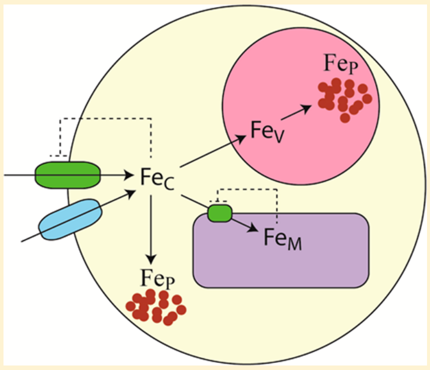

Iron plays fundamental roles in enzyme catalysis, electron transfer processes, small-molecule binding, and activation. This redox-active transition metal is found in various forms, including Fe/S clusters (ISCs), heme centers, nonheme mono- and dinuclear complexes, among others. Fe can also be deleterious to cells, as certain forms participate in Fenton chemistry that generates ROS that can, in turn, damage DNA, proteins, and membranes.[1] Like all cellular processes, Fe trafficking and metabolism are commonly considered to be tightly regulated.

The molecular-level details of Fe trafficking and regulation are best understood in the budding yeast *Saccharomyces cerevisiae*. Major "traffic hubs" in Fe metabolism include mitochondria and vacuoles, but the plasma membrane, cytosol, and nucleus also play important roles.[2,3] The plasma membrane contains numerous proteins that import Fe from the environment. The membrane-bound Fet3p/Ftr1p complex constitutes the "high-affinity" Fe importer.[4] Genes encoding these and ~20 other Fe-related proteins are controlled by Aft1p/Aft2p.[5] These transcription factors are sensitive (via a partially understood mechanism) to the concentration of unidentified Fe-containing species in the cytosol.

The cells also contain low-affinity Fe import pathways, the most important of which involves plasma-membrane protein Fet4p.[6] Fet4p is induced by Aft1p in response to low concentrations of Fe in the growth medium.[7] Plasma-membrane protein Smf1p may constitute a second low-affinity Fe importer. This divalent metal transporter primarily transports Mn, but it can also transport Fe^{II}, albeit with low affinity.[8]

Most cytosolic Fe is sent to the mitochondria as these organelles are the primary site of ISC assembly and the only site of heme biosynthesis. Cytosolic Fe used for these processes is imported via the mitochondrial inner-membrane proteins Mrs3p and Mrs4p.[9] Many of the Fe-containing prosthetic

Received: July 30, 2013
Revised: December 9, 2013
Published: December 17, 2013

dx.doi.org/10.1021/bi4010304 | *Biochemistry* 2013, 52, 9413−9425

groups that are generated in the mitochondria are installed in respiratory complexes.

Excess cytosolic Fe is transported into vacuoles. These organelles store and sequester Fe and then mobilize it as it is needed by the cell. The dominant form of Fe in the organelle is a mononuclear high-spin (HS) Fe^{III} complex with polyphosphate-related ligands.[10] Located on the vacuolar membrane, Ccc1p is the only known Fe importer of vacuolar Fe; however, Fe can also be imported into vacuoles via endocytosis.[11] Yap5p is an Fe-sensing protein that regulates the transcription of *CCC1* mRNA in response to cytosolic Fe.[12] *CCC1* mRNA is also regulated by Cth1p and Cth2p; the binding of these proteins under Fe-limited conditions destabilizes the message, thereby preventing translation.[13]

Like all biological systems, yeast cells are commonly viewed as being able to tightly regulate the import and trafficking of all cellular metabolites,[14] yet curiously, Fe continuously accumulates in such cells in glucose-containing medium for 2 months.[15] To explore this unusual phenomenon, we used Mössbauer (MB) and EPR spectroscopies, as well as ICP-MS, to monitor the Fe content of yeast grown to various stages on rich medium (YPAD) and minimal medium (MM). Exponentially growing cells maintained a constant level of cellular Fe because of a balance between cell-growth and Fe import rates. In post-exponential growth phases, Fe accumulated in the cell, mainly as Fe^{III} oxyhydroxide nanoparticles and vacuolar HS Fe^{III} species. These effects were simulated semiquantitatively by a mathematical model.

■ EXPERIMENTAL PROCEDURES

Yeast Strain and Media. The primary strain used in this study was W303 (*MATα, ura3-1, ade2-1, trp1-1, his3-11,15, leu2-3,112*). Strain DY150 (FET3-GFP::KanMX[16]), isogenic to W303, was used to visualize Fet3-GFP. Cells were grown on standard YPAD with 2% (w/v) glucose and 40 mg/L adenine hemisulfate dihydrate agar plates for 3−4 days. For liquid cultures, YPAD and MM were prepared as described previously.[17] $^{56}Fe^{III}$ or $^{57}Fe^{III}$ citrate was added to a final concentration of 40 μM. The endogenous Fe concentrations in YPAD and MM were 8 ± 3 and 0.20 ± 0.03 μM ($n = 3$), respectively.

Cell Growth and Isolation of Mitochondria. Cell stocks were prepared in 15% glycerol and stored at −80 °C. As needed, frozen cells were scraped with a sterile wooden stick and spread onto an agar plate. Single colonies were used to inoculate 50 mL of YPD medium. Once they had grown, cultures were used to inoculate 1 L of YPAD or MM such that the initial OD_{600} was ∼0.01. In the experiment measuring the cellular Fe concentration during the first 14 h of growth, 140 mL of YPD-grown cultures was used to inoculate 14 L of YPAD or MM in the fermenter. Medium glucose and cellular Fe concentrations were determined over a period of 5 days. Aliquots of cells were stored at −80 °C for Western blot analysis. For whole-cell Mössbauer studies, single colonies were directly inoculated into 1 L of medium and harvested at different times.

To isolate mitochondria, 1 L cultures were grown until the OD_{600} reached ∼1, at which point they were transferred into 24 L of MM at 30 °C in a stirred glass fermenter. The fermenter was purged with O_2 at a rate of 1 L/min. Cells were harvested after 5 days. Mitochondria were isolated in a refrigerated Ar atmosphere glovebox as described previously.[17] Anaerobic solutions were degassed on a Schlenk line prior to being brought into the box. Isolated mitochondria were packed into Mössbauer cups[18] at 18000*g* for 30 min in an ultracentrifuge (Beckman Coulter Optima L-90K) with a swinging-bucket rotor (SW 32Ti, 32000 rpm). Whole cells were similarly packed at 4000*g* for 5 min. The same spin conditions were used to pack cells into custom-made (4.2 mm outside diameter, 3.0 mm inside diameter, 80 mm length) suprasil quartz EPR tubes (Wilmad/Lab Glass, Buena, NJ). Samples were frozen in liquid N_2 for later analysis.

Metal Content Analysis. Mitochondrial and whole-cell metal concentrations were measured by ICP-MS (Agilent Corp., 7700×). Packed mitochondria and whole cells were diluted 2-fold with water; 50, 75, and 100 μL of the resulting suspensions were incubated at 95 °C overnight in 200 μL of 30% trace-metal-grade HNO_3 and 100 μL of 35% trace-metal-grade HCl (both from Fisher Scientific). Samples were then diluted with 7.7 mL of distilled−deionized water. Resulting metal concentrations were adjusted for dilution relative to the packed material and normalized using previously determined packing efficiencies of 0.70 for whole cells and 0.77 for mitochondria.[19] Reported Fe concentrations reflect those present in mitochondria and whole cells.

Glucose Assays. Glucose concentrations in growth medium were measured using the Autokit Glucose (439-90901, Wako Diagnostics) kit.[20] Culture medium was centrifuged at 16000*g* for 5 min to remove cells, and the supernatant was collected; 6.7 μL of cell-free medium was added to 1 mL of the kit assay mix. After the reaction mixture had been incubated at 37 °C for 5 min, the absorbance at 505 nm was measured, and that caused by a water blank was subtracted. Glucose concentrations in the growth medium were calculated using a standard curve, adjusting for dilution factors.

Western Blots. Fet3p expression levels were measured in membrane protein extracts essentially as described.[21] Cell pellets were resuspended in an equivalent volume of extraction buffer [150 mM NaCl, 25 mM Tris-HCl (pH 7.4), 1% (v/v) protease inhibitor cocktail (P8340, Sigma), and 1 mM phenylmethanesulfonyl fluoride] followed by an equal volume of glass beads (Biospec Inc.; 0.5 mm in diameter). The mixture was vortexed for 1 min and then cooled on ice for ≥1 min. This procedure was repeated three more times. Glass beads and unbroken cells were removed by centrifugation at 2500*g* for 5 min; then homogenates were spun at 16000*g* for 30 min at 4 °C. Pellets were resuspended in buffer containing 25 mM Tris-HCl (pH 7.4) and 1% Triton-X, and were kept at 4 °C overnight. Resultant solutions were centrifuged at 16000*g* and 4 °C for 30 min. Supernatants were collected as a clarified extract.

To determine Sod2p expression levels, whole-cell lysates were obtained as described above except that the glass beads and unbroken cells were removed by centrifugation for 10 min. Resulting supernatants were collected as a purified extract, which was assayed by the Oxyblot method as described below. Protein concentrations in extracts were measured using the BCA protein assay kit (Pierce); 60 μg of extract proteins (16 μg for Sod2p assays) was resolved via 12% sodium dodecyl sulfate−polyacrylamide gel electrophoresis (SDS−PAGE) and transferred onto polyvinylidene fluoride membranes (Bio-Rad). Membranes were blocked with 1% casein and incubated with antibodies against Fet3p and Sod2p. Antibodies against Pma1p (Abcam, ab4645), actin (Abcam, ab8224), and Pgk1p (Invitrogen, 459250) were employed as loading controls. Developed membranes were imaged (FujiFilm LAS-4000 mini), and blot densities were quantified using ImageJ

(National Institutes of Health, Bethesda, MD). Unless noted otherwise, densities were normalized to the highest-intensity band.

Oxyblot Assay. Whole-cell lysates were solubilized with 6% (w/v, final concentration) SDS and then mixed in a 1:1 volume ratio with the 2,4-dinitrophenylhydrazine solution included in the Oxyblot assay kit (Millipore). DNP-derivatized proteins were resolved by SDS−PAGE followed by Western blotting. Blot membranes were visualized using an antibody against DNP. The level of oxidative stress was quantified by densitometry.

Spectroscopy. Mössbauer spectra were recorded on MS4 WRC and LHe6T spectrometers (SEE Co., Edina, MN). Both were calibrated using α-Fe foil as described previously.[17] EPR spectra were recorded on an X-band EMX Plus spectrometer (Bruker Biospin, Billerica, MA). Spectra were rescaled on SpinCount (version 3.0.13, http://www.chem.cmu.edu/groups/hendrich/facilities/index.html) using the "T-scale" function.

■ RESULTS

We wanted to evaluate the Fe content of yeast cells grown in batch culture and harvested at exponential and post-exponential growth modes. W303 cells cultured on YPAD supplemented with 40 μM ^{57}Fe^{III} citrate grew exponentially with a doubling time (DT) of ∼1.5 h (Figure 1, circles). After ∼11 h, the growth rate started to decrease and cells underwent a transition to a slow-growing state with a DT of ∼100 h. The orange line in Figure 1 indicates the approximate time at which the transition period began; the purple line approximately demarcates the start of the slow-growth state. The glucose concentration in the culture (Figure 1B, triangles) declined exponentially during exponential growth such that the culture was virtually devoid of glucose during the slow-growth state. The observed diauxic-growth pattern undoubtedly reflects a shift from fermentation to respiration.[22]

The concentration of Fe in the growing cell was also monitored, starting four doublings (∼6 h) after inoculation (Figure 1, squares). The Fe concentration during exponential growth was 300−400 μM (measured at an OD of 0.1−1.0). In a follow-up experiment, the cellular Fe concentration was also approximately invariant during exponential growth (Figure 1C), corresponding to the first 14 h of growth. For unknown reasons, the cellular Fe concentration for this batch of cells (∼130 μM) was lower than in the first experiment, and the cells grew somewhat slower.

The cellular Fe concentration increased during the transition period (11−18 h) at a rate of ∼300 μM Fe/h (slope of the blue dashed line in Figure 1B), reached a maximum at 2−2.5 mM, and then gradually declined at a rate of approximately −4 μM Fe/h in the slow-growth state (Figure 1A, blue dashed line). With a DT of ∼100 h, this implies a constant slow-growth Fe import rate of ∼20 μM Fe/h.

We hypothesize that Fe accumulated during the transition period because of a mismatch of Fe import and cell-growth rates. This implies that the cell does not regulate these two rates perfectly. They were well-regulated (i.e., synchronized) during exponential growth, such that the cellular Fe concentration remained constant. During the transition period, the Fe import rate declined slower than the cell-growth rate declined, causing Fe to accumulate. Once the cells had reached slow-growth mode, rates were again nearly matched, such that the Fe concentration of slow-growing cells was roughly invariant with time.

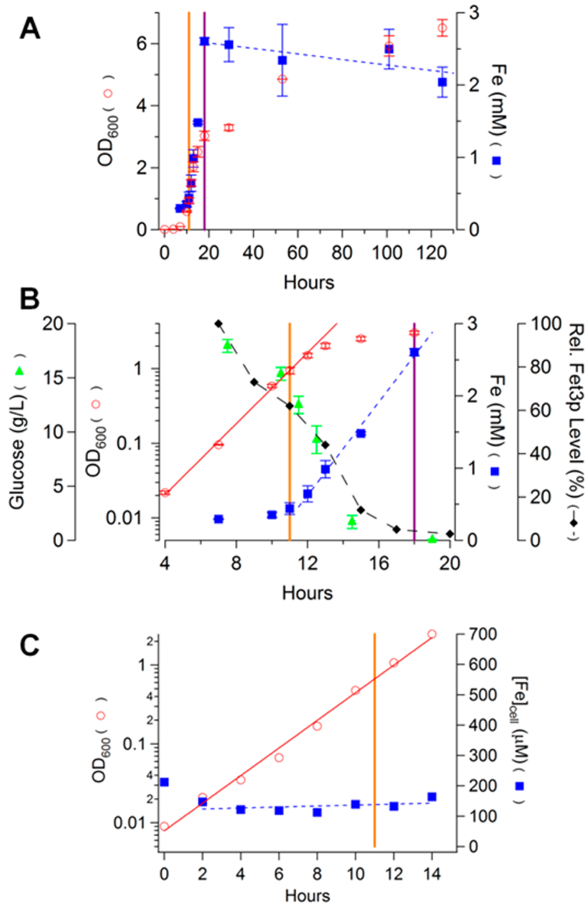

Figure 1. Chronological profile of nutrient, growth, and Fe-associated parameters for cells grown in batch culture on YPAD for 5 days: (A) full plots, (B) close-up of 4−20 h, and (C) 0−14 h for a follow-up experiment. Data include the OD$_{600}$ (circles), the cellular Fe concentration (squares), the glucose concentration (triangles), and the level of Fet3p expression (diamonds). Orange vertical lines demarcate exponential and transition modes; purple lines demarcate transition and slow-growing modes. Plotted OD$_{600}$ and iron (glucose) concentrations in panels A and B were the average of two (three) independent experiments. Bars indicate the standard deviation.

Our hypothesis accounts for these results semiquantitatively. If exponentially growing cells contained 300 μM Fe and their DT was 1.5 h, the Fe import rate should be 200 μM Fe/h. If cells stopped growing while the Fe import rate remained unchanged, they should accumulate Fe at this rate (not at a rate of ∼300 μM/h as measured). If cells grew with a DT of >1.5 h, excess Fe should still accumulate but at a slower rate. These discrepancies arise because of significant batch-to-batch variations in growth rate and Fe concentration. Nevertheless, we favor this hypothesis because of its simplicity; alternatives would seem to require that Fe import rates increase during the transition period and then decrease during the subsequent slow-growth state. This scenario seems more complicated and less intuitive.

The Fet3p expression level, which reflects the activity of the high-affinity Fe import system, was also monitored. The level of expression was maximal during exponential growth but declined gradually during the transitionary period and became undetectable during the slow-growth period (Figure 1B, diamonds, and Figure S1A of the Supporting Information). These changes can also be explained by our hypothesis, namely that Fe enters exponentially growing cells primarily through the high-affinity plasma-membrane Fe import system. Because Fet3p is essentially not expressed during the slow-growth mode, the slow-growth Fe import rate probably reflects one or more low-affinity Fe import systems.

The same parameters were monitored for cells grown on MM. These cells grew more slowly during the exponential phase (DT ≈ 2.0 h) (Figure 2, circles). They underwent a transition at an OD_{600} of ≈2 to a true stationary state rather than to a slow-growth state. MM-grown cells consumed glucose more slowly, but the development of the transition period still correlated with a decline in glucose concentration (Figure 2B, triangles). The Fe concentration in exponentially growing MM cells (~400 μM measured at an OD of 0.2) was similar to that observed for YPAD-grown cells, while the rate of maximal Fe import during the transition period (100 μM/h) was lower (slope of the blue dashed line in Figure 2B). In a follow-up experiment, we observed that the Fe level was almost invariant during the initial 10 h of growth (Figure 2C).

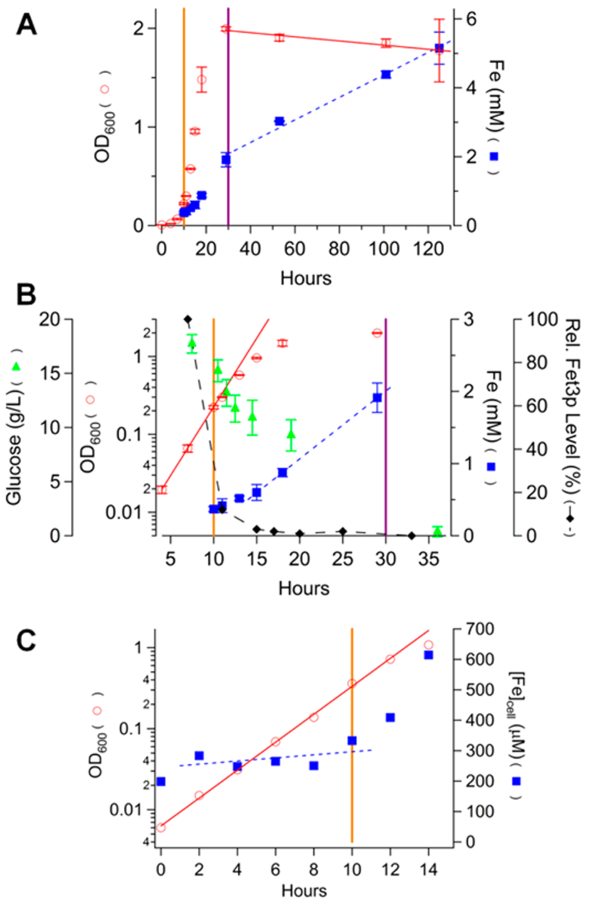

Figure 2. Chronological profile of nutrient, growth, and Fe-associated parameters for cells grown in batch culture on MM for 5 days: (A) full plots, (B) close-up of 5−35 h, and (C) 0−14 h for a follow-up experiment. Data symbols and lines are the same as in Figure 1. Reported OD_{600} and iron (glucose) concentrations in panels A and B were the average of two (three) independent experiments. Bars indicate the standard deviation.

Our hypothesis can again account for these results semiquantitatively. A DT of 2 h and an Fe concentration of 400 μM in exponentially growing cells imply an Fe import rate of 200 μM/h, double the observed rate. Nevertheless, we continue to favor our hypothesis because alternatives are more complex and less intuitive.

The Fe concentration of MM-grown cells that just entered the stationary state was ~2 mM, similar to that of YPAD-grown cells. Unlike the case for YPAD-grown cells, Fe continued to accumulate in MM-grown cells when they were in the stationary state, such that they contained ~5 mM Fe after ~100 h in this state. This corresponded to an average rate of ~30 μM Fe/h. This stationary-state Fe import rate was similar to the slow-growth Fe import rate of YPAD-grown cells. Both probably originated from Fe entering via a low-affinity Fe import system that likely dominates during post-exponential growth modes.

The level of Fet3p expression in MM-grown cells was maximal during exponential growth and declined rapidly thereafter (Figure 2B, diamonds, and Figure S1B of the Supporting Information). With 40 μM Fe in the medium, we find it remarkable that the high-affinity Fe import system was expressed at all; no Fet3p expression was previously observed in MM-grown cells harvested during the late exponential or early transition phase (OD ~ 1.2).[23] When cells are grown in Fe-adequate medium, the high-affinity system might be expressed only during early exponential growth. Our hypothesis can explain the faster rate of FET3 shutdown along with the slower rate of growth shutdown and a similar concentration of Fe in YPAD- and MM-grown cells at the end of the transition period. Accordingly, shut-down of the high-affinity import system and the cell-growth rate are probably better synchronized in MM-grown cells.

As a loading control, we used Pma1p, an ATPase that is typically used as a plasma-membrane marker (Figure S1 of the Supporting Information). However, its expression level varied with harvest time. We loaded the same amount of protein into each lane based on measured protein concentrations such that blot densities from one lane to another can be compared.

In contrast to Fe, neither Cu, Mn, nor Zn ions accumulated in 1- or 5-day-old YPAD or MM cells. The concentration of Zn actually declined during the transition from exponential to slow- or stationary-growth modes (Figure S2 of the Supporting Information). This decline was gradual in YPAD cells and was preceded by a spike in concentration (Figure S2 of the Supporting Information, squares). In MM cells, there was no spike and the decline was more dramatic (Figure S2 of the Supporting Information, circles). We have not established the molecular basis for these effects. However, if yeast cells contain a Zn efflux pump (e.g., homologous to ZnT1, a mammalian Zn efflux protein[24]), it may be activated during post-exponential growth. Alternatively, Zn influx pathways may shut down as cell growth slows.

We next used Mössbauer (MB) spectroscopy to evaluate the form(s) of Fe that accumulated in yeast grown to high culture densities on YPAD and MM. The 5 K low-field MB spectrum of YPAD-grown cells harvested in the early transition phase (OD = 2.1) (Figure 3A) was dominated (79% of spectral intensity) by a sextet assigned to the mononuclear HS Fe^{III} species located in vacuoles.[10] The brown line above the spectrum simulates this feature.

The spectrum also exhibited a quadrupole doublet from nonheme high-spin (NHHS) Fe^{II} ions (8%, purple line) and the so-called central doublet or CD (9%, green line). The latter feature arises from $S = 0$ $[Fe_4S_4]^{2+}$ clusters and low-spin (LS)

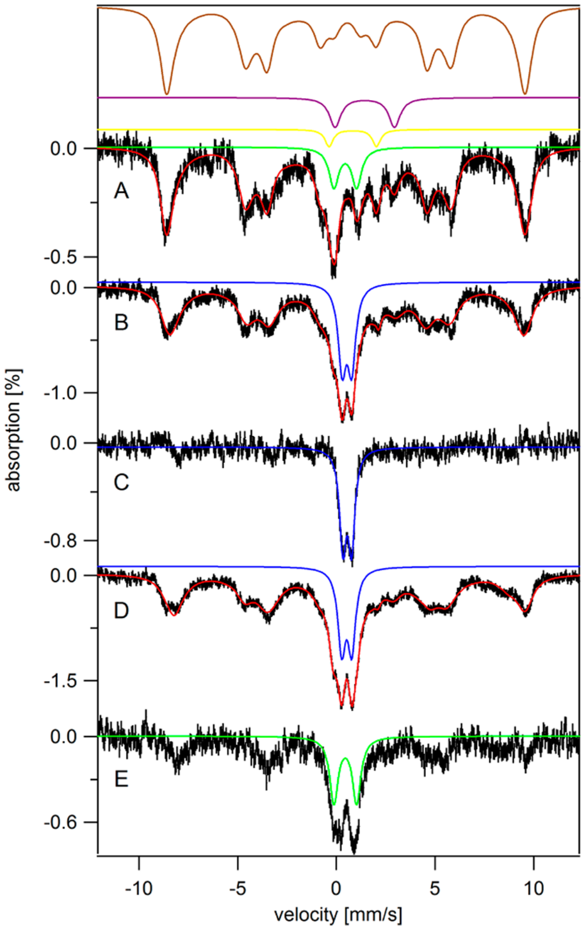

Figure 3. Mössbauer spectra (5 K, 0.04 T) of whole yeast cells grown on YPAD and harvested at various time points: (A) early transition phase (OD of 2.1), (B) late transition phase (OD of 3.2), (C) B-minus-A difference spectrum, (D) postdiauxic-growth phase (OD of 8.0), and (E) D-minus-B difference spectrum. Red lines simulate collectively the spectral features associated with HS Fe^{III}, NHHS Fe^{II}, HS Fe^{II} heme, CD, and Fe^{III} nanoparticles. Brown, purple, yellow, green, and blue lines are simulations of HS Fe^{III}, NHHS Fe^{II}, HS Fe^{II} heme, the central doublet, and Fe^{III} nanoparticles, respectively. The field was applied parallel to γ-rays.

heme Fe^{II} ions (the two types of species cannot be distinguished).[25] A minor contribution from HS Fe^{II} hemes (3%, yellow line) could also be discerned. The CD and heme components are due primarily to mitochondrial respiratory complexes. The location of the NHHS Fe^{II} species has not been established. Fitting parameters and associated cellular Fe concentrations are listed in Table S1 of the Supporting Information.

The MB spectrum exhibited by YPAD-grown cells harvested in the late transition period (OD of 3.2) exhibited the same general features (Figure 3B), as well as a new quadrupole doublet (19%, blue line) with parameters ($\delta \approx 0.53$ mm/s, and $\Delta E_Q \approx 0.50$ mm/s) typical of Fe^{III} phosphate/polyphosphate-associated oxyhydroxide nanoparticles. The Fe concentration of these cells (1.0 mM) was higher than those harvested at an OD of 2.1 (0.7 mM). The bulk of the additional Fe was present as nanoparticles, as evidenced by the difference spectrum of Figure 3C.

YPAD-grown cells harvested 3 days later in the slow-growth state (OD of 8.0) exhibited a similar MB spectrum (Figure 3D) but with an ~50% higher percent effect, consistent with the higher concentration of Fe in the sample (1.5 mM). The difference spectrum (Figure 3E, slow growth minus transition) revealed that the Fe that accumulated during this period was mainly in the form of the CD and mononuclear HS Fe^{III}. The absolute concentration of CD-associated Fe in YPAD-grown slow-growth cells was twice that in transition cells (Table S1 of the Supporting Information). The generation of more mitochondrial Fe for cells in the slow-growth phase is consistent with the greater use of respiratory complexes after the diauxic shift.

The MB spectrum of MM-grown cells harvested in exponential phase (OD of 0.2) exhibited a distribution of Fe similar to that in YPAD-grown cells, except that the percentage of Fe due to the CD was slightly higher (15% of spectral intensity) (Figure 4A). MM-grown cells harvested at later

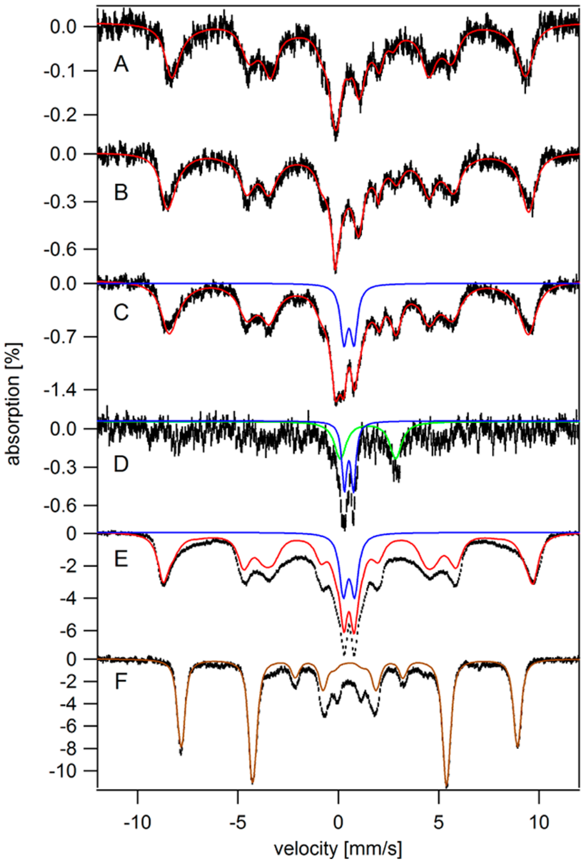

Figure 4. Mössbauer spectra of whole yeast cells grown on MM and harvested at various time points. For spectra A–E, the temperature was 5 K and a 0.04 T field was applied parallel to γ-rays. For spectrum F, the temperature was 4.2 K and a 6 T field was applied perpendicular to the γ-rays: (A) early exponential phase (OD of 0.2), (B) late exponential phase (OD of 1.2), (C) transition phase (OD of 1.8), (D) C-minus-B difference spectrum (the intensity of spectrum B was doubled and then subtracted from spectrum C), (E) stationary phase (OD of 1.8; growth for 5 days), and (F) sample equivalent to that used for spectrum E (OD of 1.7; growth for 5 days). Red lines are composite simulations that include contributions from HS Fe^{III}, NHHS Fe^{II}, HS Fe^{II} heme, CD, and Fe^{III} nanoparticles. Blue and green lines simulate contributions from Fe^{III} nanoparticles and HS Fe^{II}, respectively. The brown line simulates the HS Fe^{III} species using the following values: $S = {}^5/_2$, $D = 0.15$ cm^{-1}, $E/D = 0.21$, $A_0/g_N\beta_N = -233$ kG, $\delta = 0.55$ mm/s, $\Delta E_Q = 0.42$ mm/s, and $\eta = 1.3$.

stages of exponential growth (Figure 4B, OD of 1.2) exhibited virtually the same spectrum. This is evidence that the distribution of Fe in the cell is constant during the exponential-growth phase. A similar distribution has been reported for cells harvested toward the end of exponential growth (OD of ~1.0).[23,26]

The Fe distribution of MM-grown cells changed as the cells moved into the transition phase (Figure 4C). The overall spectral intensity increased because of the higher Fe concentrations in these cells. The difference spectrum (Figure 4D, transition minus exponential) revealed that $\mathrm{Fe^{III}}$ nanoparticles and NHHS $\mathrm{Fe^{II}}$ ions (and some mononuclear HS $\mathrm{Fe^{III}}$ ions) mainly accumulated. This caused the percentage of Fe due to the CD in these spectra to decline; however, the absolute concentration of the CD increased somewhat.

The MB spectrum of cells grown in MM for 5 days in the stationary phase (Figure 4E) was intense, consistent with the tremendous buildup of Fe evident in Figure 2 at 120 h. The primary form of Fe that accumulated was mononuclear HS $\mathrm{Fe^{III}}$ originating from vacuoles. The absolute concentration of $\mathrm{Fe^{III}}$ nanoparticles also increased, but there was no increase in its percentage.

After the contributions had been removed from these two dominating components (and the CD), the residuals revealed some broad unresolved absorption corresponding to the difference between the black hashmarks and the red line in Figure 4E. We recorded a 100 K spectrum in hopes that this feature would collapse into a doublet, as is observed for ferritin,[27] but it did not (Figure S3 of the Supporting Information). This suggests a somewhat higher blocking temperature for the associated particles. We recorded the low-temperature high-field (6 T) MB spectrum of an equivalent sample (Figure 4F) to overcome any spin−spin interaction due to the high Fe concentration and to better characterize this elusive species. However, the spectrum was dominated (72% of the overall intensity) by the HS $\mathrm{Fe^{III}}$ sextet, such that the less intense, broad unresolved feature could not be characterized.

The EPR spectrum of an equivalent sample (WT cells grown in MM for 5 days harvested at the stationary phase) provided additional characterization of the broad unresolved species. The spectrum exhibited a derivative-like $g \sim 2.0$ feature along with an intense $g = 4.3$ signal (Figure 5A). The latter signal arose from the HS $\mathrm{Fe^{III}}$ species whose sextet dominated the MB spectrum of Figure 4E. The $g \sim 2$ signal probably arose from the same species that exhibited the broad unresolved MB feature. The EPR signal was reminiscent of that originating from $\mathrm{Fe^{III}}$ phosphate/polyphosphate-associated oxyhydroxide nanoparticles present in mitochondria of various ISC mutants.[17,28] However, the line shape and temperature dependence were somewhat different. Like the EPR signal of ISC mutant nanoparticles, the new signal exhibited inverse Curie law behavior. The effect was less dramatic relative to that of the ISC mutant signal, but the Curie law behavior of the $g = 4.3$ signal allowed us to use it as an internal standard. Although much remains to be learned with regard to the broad unresolved MB species that gives rise to the $g \sim 2$ EPR signal, we suggest that it arises from a somewhat different form of $\mathrm{Fe^{III}}$ nanoparticles relative to that present in ISC mutant mitochondria.[17,28,29]

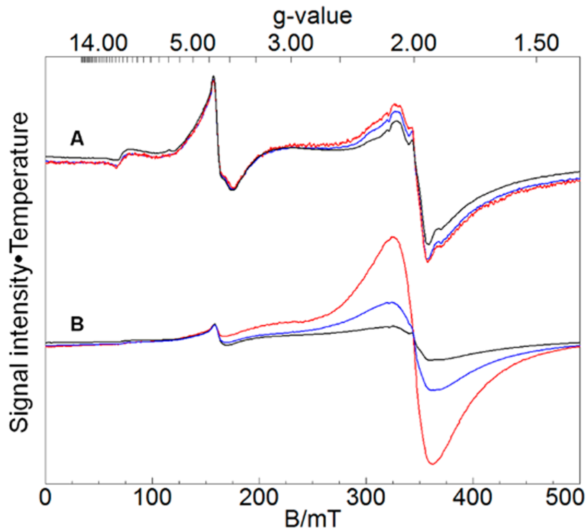

Figure 5. X-Band EPR spectra of cells grown for 5 days (A) on MM with 40 μM Fe and (B) on MM with 400 μM Fe: black, 10 K; blue, 30 K; red, 80 K. Spectra were recorded at a microwave power of 0.05 mW, a frequency of 9.64 GHz, and a modulation amplitude of 10 G and then were adjusted vertically so that the $g = 4.3$ resonances would be aligned. Spectral intensities in panels A and B were multiplied by the absolute temperature, while those in panel A were additionally multiplied by 5 for the purpose of presentation.

The MB spectrum of cells grown on MM that contained 400 μM ^{57}Fe (10 times greater than normal) was more intense than the corresponding spectrum of cells grown with 40 μM ^{57}Fe in the medium; the spectral line shape was also different (Figure 6A). The MM sample grown on 400 μM ^{57}Fe contained ~28 mM Fe, ~3.5 times higher than the Fe concentration of cells grown on MM that contained 40 μM ^{57}Fe. Approximately half of the spectral intensity was due to a broad doublet in the center of the spectrum, indicating ISC mutant-type nanoparticles. Approximately 9% of the spectral intensity was due to mononuclear HS $\mathrm{Fe^{III}}$ species. Subtracting these two features from the spectrum revealed a broad unresolved magnetic feature between −5 and 7 mm/s representing ~30% of the original spectral intensity (Figure 6B). This feature was similar to the less intense broad unresolved feature in Figure 4E that could not be characterized well. The 6 T MB spectrum (Figure 6C) was again broad and poorly resolved. Approximately 90% of the spectral intensity arose from $\mathrm{Fe^{III}}$ nanoparticles, with the remaining intensity being due primarily to mononuclear HS $\mathrm{Fe^{III}}$. The HS $\mathrm{Fe^{III}}$-subtracted difference spectrum (Figure 6D, hashmarks) revealed broad absorption, though the spectrum was distinct from the 6 T MB spectrum of mitochondrial nanoparticles (Figure 6D, dotted line). We are unable to decompose the spectrum further but conclude that the sample grown on MM supplemented with 400 μM ^{57}Fe contained more than one type of $\mathrm{Fe^{III}}$ oxyhydroxide nanoparticle. The X-band EPR spectrum of an equivalent sample (Figure 5B) exhibited an intense broad $g \sim 2$ signal that again displayed inverse Curie law behavior. The line shape and temperature dependence of this signal differed from those of the signal present in spectra of nanoparticles found in ISC mutant mitochondria, again indicating different magnetic properties and thus different structures and compositions. The signal is similar to that exhibited by cells grown in MM for 5 days on 40 μM ^{57}Fe.

Mitochondria were isolated from cells grown in MM for 5 days in the stationary state to determine whether they contained nanoparticles. The yield was low because the cell walls were thick and difficult to break. The sample exhibited the MB spectrum shown in Figure S4 of the Supporting

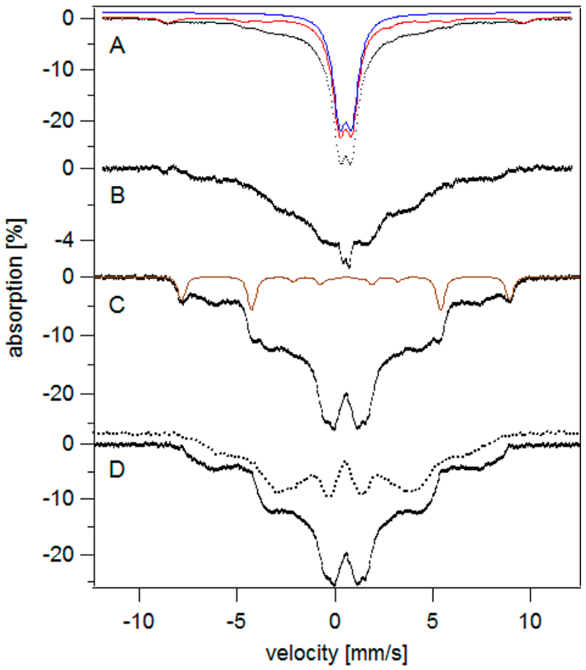

Figure 6. Mössbauer spectra of MM-grown yeast cells at the stationary phase. (A) Cells grown in MM containing 400 μM Fe at the stationary phase (OD of 2.2, growth for 5 days). The red line simulates the contributions from HS Fe^{III}, Fe^{III} nanoparticles, and the CD. The blue line simulates the ISC mutant-type nanoparticles. (B) Same as panel A but after subtraction of the red line simulation. For panels A and B, the temperature was 5 K and a 40 mT field was applied parallel to the γ-rays. (C) Same as panel A but at 6 T (transverse field) and 4.2 K. The brown line simulates the HS Fe^{III} contribution. (D) Same as panel C but the HS Fe^{III} component has been subtracted. The dotted line is the equivalent MB spectrum of isolated mitochondria from Aft1-1^{up} cells.[19]

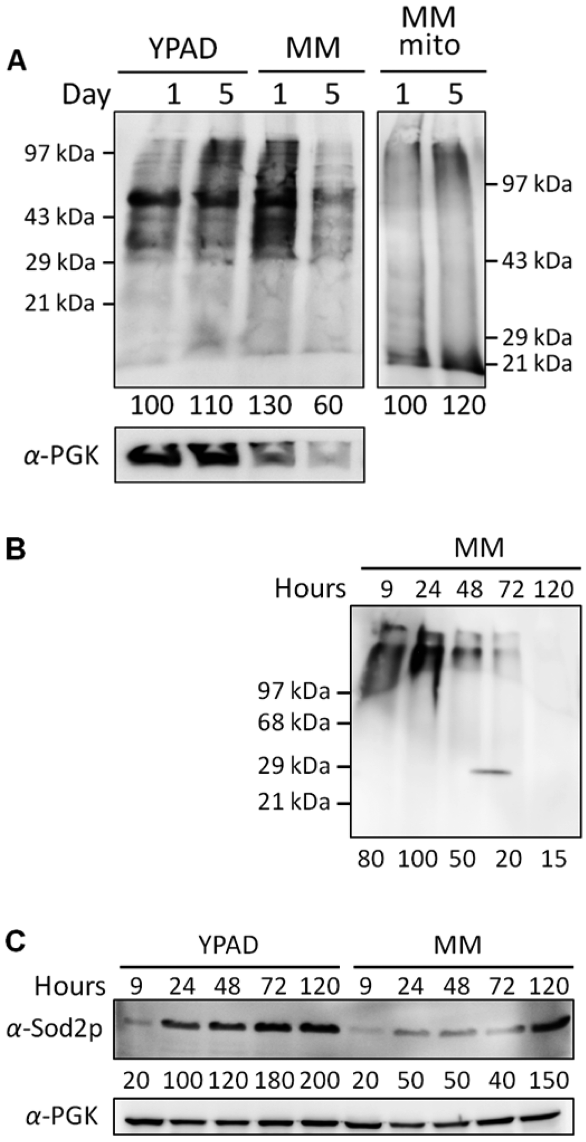

Figure 7. Oxyblot and Western blot against Sod2p of whole cells and mitochondria harvested under different conditions. (A) Oxyblot of whole-cell lysates (left) and mitochondrial extracts (right). The medium and days of growth are displayed atop the blots. Overall band intensities (below the blots) are indicated as percentages relative to YPAD/1 day (left) or MM/1 day (right) blots. (B) Oxyblot time course of whole-cell lysates grown on MM. Band intensities (below the blots) are indicated as percentages relative to that of the MM/24 h blot. The intensity at ~29 kDa between lanes 3 and 4 is an artifact. (C) Western blot against Sod2p for YPAD and MM cells grown for different times (same MM samples as in panel B): lanes 1−5, YPAD; lanes 6−10, MM; hours of growth given atop each lane. Band intensities (below the blots) are given as percentages relative to that of the YPAD/1 day blot. Each lane was developed with 4 μg (Oxyblot for whole-cell lysates), 15 μg (Oxyblot for mitochondrial extracts), and 16 μg (Western blot against Sod2p for whole-cell lysates) of protein.

Information. The overall percent effect was very low, with ~40% of the spectral intensity due to nanoparticles and ~45% due to the CD and possibly with a small contribution from $[Fe_2S_2]^{2+}$ clusters.[23] Although a substantial percentage of the Fe in these mitochondria was present as nanoparticles, the amount was far smaller (in terms of percentage and absolute concentration) than the amount of nanoparticles that accumulate in ISC mutant mitochondria.[17,28,29] Thus, nanoparticles do not accumulate in stationary-state WT mitochondria to anywhere near to the extent that they do in mitochondria from ISC mutant strains. We conclude that the majority of nanoparticles present in whole WT cells grown in MM for 5 days harvested in the stationary state are not located in mitochondria.

Oxidative Stress in Post-exponential Cells. Cells grown on YPAD for 5 days exhibited a level of oxidative damage similar to that of cells grown on the same medium for 1 day (Figure 7A, lane 2 vs lane 1). This was unexpected given the higher Fe concentration in the 5-day-old cells. Cells grown on MM for 5 days actually experienced less oxidative damage than comparable 1-day-old cells (Figure 7A, lane 4 vs lane 3). This was also unexpected because MM-grown cells in the stationary state contained much higher Fe concentrations than did MM-grown cells harvested in exponential and transition phases.

As loading controls, we tried 3-phosphoglycerate kinase (PGK1) and actin for whole-cell extracts and porin for mitochondrial extracts (Figure 7 and Figure S5 of the Supporting Information). However, none was ideal, because their expression levels varied with harvest time. PGK1 varied less than the others, so we show it in Figure 7. As with the Oxyblot band of lane 4, the loading control also showed a decline at 5 days relative to 1 day, raising the question of whether 5-day-old cells had less oxidative damage than 1-day-old cells, or approximately the same level. A second experiment (Figure 7B) indicated a decrease in the level of oxidative damage as MM-grown cells aged during the stationary period, and in this experiment, the loading control was better behaved (Figure 7C). Thus, it appears that cells grown in MM for 5 days suffer less ROS damage than 1-day-old cells, a result that differed from our expectations. Also unexpected was the more general conclusion of this study, namely that the cellular Fe concentration is not an accurate predictor of ROS damage. The metabolic activity, the growth medium, and the duration of growth may also be important factors.

We wondered whether the higher ROS level in slow-growing YPAD cells, relative to that in stationary-state MM cells, resulted because the YPAD cells were respiring (and thus generating more ROS), whereas 5-day-old MM cells were less metabolically active. Might MM-grown cells be unable to undergo the diauxic shift and respire because of a lack of essential nutrients present in YPAD but absent in MM? Cellular Sod2p levels are upregulated during the diauxic shift.[30] To examine whether MM cells also underwent this shift, we quantified the level of Sod2p in YPAD versus MM cells. While the cells were growing for 5 days, Sod2p band intensities in both YPAD and MM cells gradually increased (Figure 7C). The Sod2p level in slow-growing YPAD cells was increased 10-fold relative to that in the same cells during exponential growth (Figure 7C, YPAD, 120 h vs 9 h). The Sod2p level in MM cells also increased, in this case by 7.5-fold, between the exponential and stationary phases (Figure 7C, MM, 120 h vs 9 h). We conclude that like YPAD cells, MM cells also shift their metabolism from fermentation to respiration when the level of glucose is depleted. This is supported by the slightly increased level of oxidative stress in mitochondria isolated from 5-day-old versus 1-day-old MM cells (Figure 7A, lane 6 vs lane 5). However, we still do not have a good explanation for why 5-day-old MM cells suffered less ROS damage than 1-day-old MM cells; perhaps metabolic activity declined while ROS damage repair processes remained highly active.

Model Development. We have developed a chemically based mathematical model to help interpret our results. In it, cellular Fe (Fe_{cell}) was divided into four components, including cytosolic (Fe_C), vacuolar (Fe_V), and mitochondrial (Fe_M) iron and nanoparticles (Fe_P); thus, $[Fe_{cell}] = [Fe_V] + [Fe_M] + [Fe_C] + [Fe_P]$. We wanted to simulate concentrations of each component and compare them to the concentration data obtained from our MB, EPR, and ICP-MS studies. To do this, we first assigned each component of the model to an observed species. Fe_V was assigned to the vacuolar HS Fe^{III} species, Fe_M to the sum of the central doublet Fe and heme Fe (most of which is associated with mitochondria), and Fe_C to the observed NHHS Fe^{II} species. Fe_P was assigned to the sum of both types of nanoparticles that were observed. Two versions of the model were developed so that two possible locations of nanoparticles could be considered. In version C, nanoparticles were presumed to be generated in the cytosol from Fe_C, whereas in version V, they were assumed to be generated in vacuoles from Fe_V. In both versions, the rate of nanoparticle formation was proportional to either $[Fe_C]$ or $[Fe_V]$ raised to the power *px*.

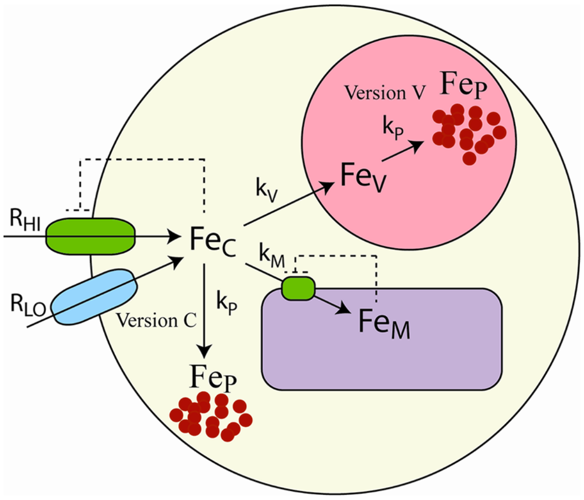

Figure 8. Model of Fe trafficking in yeast cells. Fe from the medium enters via high-affinity (R_{HI}) and low-affinity (R_{LO}) pathways. R_{LO} is unregulated, while R_{HI} is regulated by the concentration of cytosolic Fe ($[Fe_C]$), indicated by the dashed lines. Fe_C moves into the mitochondria and vacuoles, forming mitochondrial (Fe_M) and vacuolar (Fe_V) forms. The import of Fe_C into the mitochondria is regulated by the concentration of Fe_M. In version C, Fe^{III} nanoparticles (Fe_P) were assumed to form in the cytosol, whereas in version V, they were assumed to form in vacuoles. Rate constants and other parameters are listed in Table 1.

The chemical model (Figure 8) assumed two Fe import pathways called HI (high affinity) and LO (low affinity), with import fluxes R_{HI} and R_{LO}, respectively. Imported Fe, assumed to be Fe_C, was transported to mitochondria and vacuoles at independent rates. The simulated $[Fe_C]$ resulted from a balance among the rates of Fe import, the rates of export of Fe into these two organelles, and cell-growth rate α. For version C, these chemical processes were included in the ordinary differential equations (ODEs)

$$\frac{d[Fe_C]}{dt} = R_{HI}\left[\frac{1}{1 + \left(\frac{[Fe_C]}{K_C}\right)^{cs}}\right] + R_{LO} - k_M\left[\frac{1}{1 + \left(\frac{[Fe_M]}{K_M}\right)^{ms}}\right][Fe_C] - k_P[Fe_C]^{px} - (k_V + \alpha)[Fe_C]$$

$$\frac{d[Fe_V]}{dt} = k_V[Fe_C] - \alpha[Fe_V]$$

$$\frac{d[Fe_M]}{dt} = k_M\left[\frac{1}{1 + \left(\frac{[Fe_M]}{K_M}\right)^{ms}}\right][Fe_C] - \alpha[Fe_M]$$

$$\frac{d[Fe_P]}{dt} = k_P[Fe_C]^{px} - \alpha[Fe_P]$$

which describe the changes in the concentrations of each Fe component in the model. A similar set of ODEs was constructed for version V (Figure S6 of the Supporting Information), with similar results.

The rate of Fe import via LO was considered to be constant under all growth conditions, whereas HI was homeostatically regulated by the function

$$\mathrm{Reg\_}(Fe_C, K_C, cs) = \frac{1}{1 + \left(\frac{[Fe_C]}{K_C}\right)^{cs}}$$

Table 1. Parameters for Simulations[a]

	$[Fe_{cell}]$	$[Fe_C]$	$[Fe_M]$	$[Fe_P]$	$[Fe_V]$	k_V (h^{-1})	k_M (h^{-1})	α (h^{-1})
YPAD, early exponential	300_D	24_D	40_D	0_D	236_D	4.8	0.8	0.65
	314_C	32_C	40_C	5_C	234_C			
	310_V	32_V	40_V	1_V	237_V			
YPAD, late exponential	700_D	56_D	90_D	0_D	550_D	4.8	0.8	0.29
	677_C	33_C	89_C	11_C	553_C			
	667_V	33_V	84_V	7_V	543_V			
YPAD, slow growth	1500_D	75_D	150_D	285_D	990_D	0.43	0.60	0.034
	1577_C	79_C	150_C	288_C	986_C			
	1359_V	90_V	152_V	128_V	989_V			
MM, exponential	430_D	13_D	90_D	0_D	327_D	5.2	1.6	0.50
	454_C	31_C	89_C	6_C	327_C			
	450_V	32_V	89_V	2_V	327_V			
MM, stationary for 24 h	1500_D	180_D	135_D	165_D	1020_D	0.90	0.16	0.00
	1367_C	61_C	132_C	147_C	1027_C			
	1284_V	65_V	135_V	40_V	1044_V			
MM, stationary for 120 h	8100_D	170_D	130_D	2000_D	5800_D	0.90	0.16	0.00
	7698_C	61_C	185_C	1173_C	6279_C			
	6993_V	65_V	187_V	2077_V	4664_V			

[a] Most of the composite data were obtained from the simulated percentages of MB spectra in Figures 3 and 4. Composite data of YPAD cells in the early exponential-growth mode were estimated by assuming that the Fe distribution in the cells was identical to that in the YPAD cells in the late exponential-growth mode. Subscripts: D, composite data; V, version V; C, version C. Concentrations are in micromolar. Parameters: R_{HI} = 330 μM/h, R_{LO} = 30 μM/h, K_C = 30 μM, cs = 3, K_M = 115 μM, and ms = 8. For version C, px = 1.4 and k_P = 0.034 h^{-1}. For version V, px = 1.3 and k_P = 0.0006 h^{-1}.

Reg_ functions can be used as surrogates for regulatory processes for which the molecular details are not known or are overly complicated.[31] These functions allow regulation to be described by just three parameters, including the sensed form of Fe, the threshold concentration, and the sensitivity of the regulatory effect. In our model, two Reg_ functions were employed, one that regulated the rate of import of Fe into the cell and another that regulated the rate of import of Fe into mitochondria. For the first, we assumed that Fe_C was the sensed form of Fe, K_C was the threshold concentration, and cs was the sensitivity. Because of this function, the Fe import rate through HI declines when $[Fe_C] > K_C$ and increases when $[Fe_C] < K_C$. For the second Reg_ function, we assumed that Fe_M was the sensed form of Fe that regulates mitochondrial import, with threshold K_M and sensitivity factor ms.

Both C and V sets of ODEs were solved numerically using Maple 17 (Maplesoft Inc.), but this could only be done after values for all 11 associated parameters (R_{HI}, R_{LO}, k_M, k_V, k_P, K_C, cs, K_M, ms, px, and α) had been assigned. Finding best-fit values involved an iterative fitting procedure. The data in Table 1 were the composite of results rather than raw data from any particular sample. An error function was developed for quantitative comparisons among the 24 data points of Table 1 (6 conditions × 4 Fe component concentrations) and the corresponding simulated concentrations. Parameter values were first guesstimated and then adjusted systematically to minimize this function. Parameters were divided into those that were common for both versions and all conditions of the model (R_{HI}, R_{LO}, K_C, cs, K_M, and ms) and those that differed for different versions (k_P and px) and conditions (k_M, k_V, and α). Best-fit parameter values and simulated concentrations are listed in Table 1.

The Fe speciation in YPAD and MM cells growing under exponential-growth and slow-growth/stationary-state conditions was simulated (Figure 9). The first 5 h of the simulation reflects exponential growth, while the next 115 h reflects slow growth for YPAD cells (Figure 9A,B) and the stationary-state condition for MM cells (Figure 9C,D). These plots should be semiquantitatively compared to those in Figures 1 and 2, respectively. Simulated changes in Fe concentrations probably occurred more slowly than in real cells because the simulated Fe import and cell-growth rates were adjusted simultaneously at 5 h. In real cells, the growth rate declines quickly while the Fe import rate declines more slowly. The black dashed line in Figure 9B illustrates this effect in the extreme. Here, the growth rate was adjusted to zero at 5 h while the Fe import rate was maintained exponential-growth conditions. The resulting increase in cellular Fe concentration was dramatic; the accumulation of Fe was more rapid than that observed in real cells.

DISCUSSION

Lack of Regulation of Iron in Post-exponential Cells.

Our results and analysis demonstrate that Fe import in yeast is effectively unregulated when cells grown in batch culture undergo a transition to post-exponential growth states. Excess Fe accumulated in cells during the transition to either a slow-growth postdiauxic state (for growth on YPAD medium) or a true stationary state (for growth on MM medium). Fe continued to accumulate in MM-grown cells in the stationary state. YPAD-grown cells probably also imported excess Fe in the slow-growth state, but this effect was counterbalanced by a non-zero growth rate. This evidence of unregulated Fe import is surprising, given the abundant evidence and commonly held assumption that all metabolites and components of a cell are tightly regulated under all growth conditions. This study shows that iron is an exception to this rule.

Several molecular-level phenomena may collectively give rise to this exceptional behavior. The low-affinity Fe import pathway dominates in postexponential cells, and the pathway does not appear to depend strongly on the growth rate of the

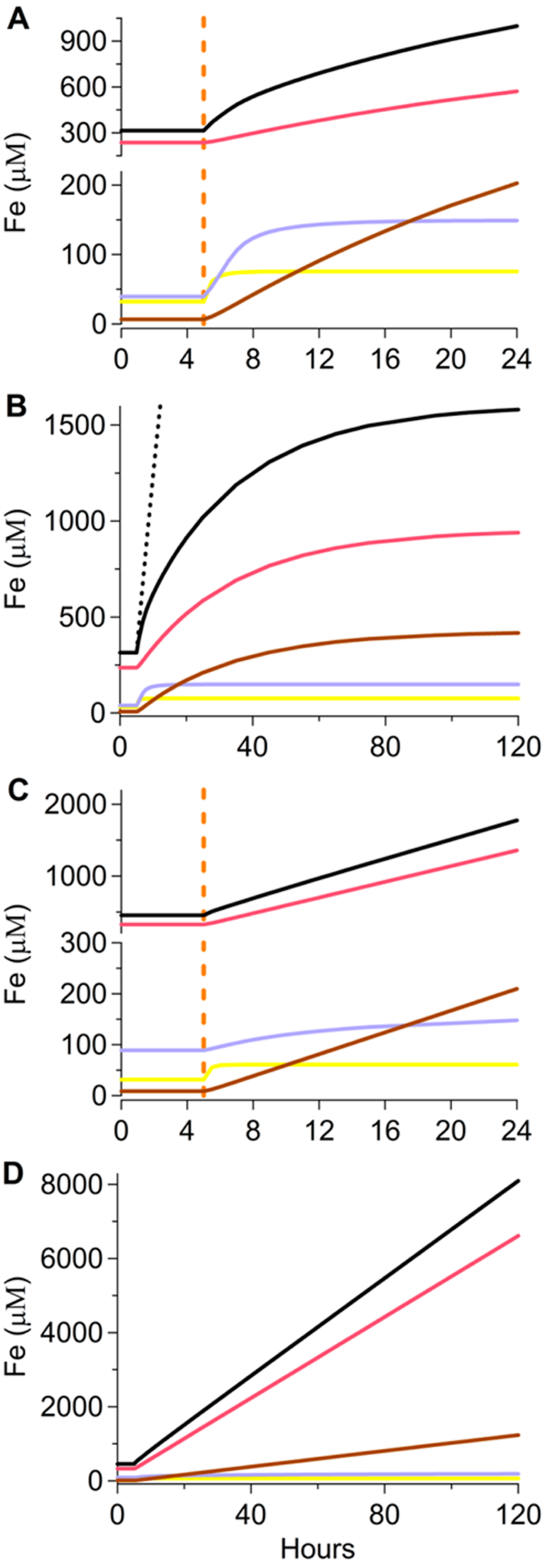

Figure 9. Simulated kinetics of Fe uptake and trafficking in yeast cells: (A) YPAD, 1-day-growth scale; (B) YPAD, 5-day-growth scale; (C) MM, 1-day-growth scale; and (D) MM, 5-day-growth scale. The first 5 h (before the orange line) reflects exponential-growth conditions, while the remaining 115 h indicates slow-growth and steady-state modes. Black, pink, cyan, yellow, and brown lines indicate [Fe_{cell}], [Fe_V], [Fe_M], [Fe_C], and [Fe_P], respectively. The dashed line simulates [Fe_{cell}] when cell growth was set to zero while Fe import rates were set to those for exponential growth.

cell. Thus, even as cells grow slowly or stop growing, they continue to import Fe through this pathway.

This is certainly one means by which the cell does not regulate the import of Fe. However, the rate of Fe import by the low-affinity pathway is probably too slow to be primarily responsible for the strong accumulation of Fe observed during the transition period; the high-affinity pathway must also be (somehow) misregulated. The high-affinity Fe import pathway is operational and tightly regulated during exponential growth, as evidenced by the strong Fet3p expression and invariant cellular Fe concentration. We hypothesize that the high-affinity pathway shuts down during post-exponential growth more slowly than the cell's growth rate declines. As a result of this mismatch, Fe accumulates in the cell.

But why did the high-affinity import pathway not shut down under post-exponential growth conditions as the rate of cell growth declined? What went wrong? According to our results and simulations, this happened because the concentration of cytosolic Fe in exponentially growing cells did not increase as cells underwent the transition to slow or stationary states. Had this happened, the Reg_ "valve" would have shut down Fe import.

But why did the Fe_C concentration not increase as cell growth slowed and Fe started to accumulate? We hypothesize that this was because much of the extra imported cytosolic Fe was converted (directly or indirectly) into nanoparticles. The cell cannot sense these aggregated precipitates and thus cannot regulate their formation. (In fact, the extent of nanoparticle formation is "contra-regulated", meaning that as the rate of Fe import declined in post-exponentially grown cells in response to cellular regulation, the rate of nanoparticle formation actually increased.) Nanoparticles are a "sink" for Fe; they remove Fe_C from the cytosol, creating a deficiency of this sensed form of cellular Fe. Thus, even as the effect of dilution became weaker (because of a decrease in the rate of cell growth), [Fe_C] did not increase and Reg_ did not shut down. The situation was different for cells growing exponentially. Here Fe import and trafficking were well-regulated and controlled because few nanoparticles formed. Fe uptake and cell-growth rates were matched such that the cellular Fe concentration was essentially invariant.

Our simulations provided quantitative support for this effect. In both early and late stages of exponential growth, the rates of import of Fe into YPAD cells were unchanged. This was certainly true for R_{LO} but also for R_{HI}. The Fe import rate through HI is given by the product of R_{HI} and Reg_. In our simulations, R_{HI} was fixed for all conditions at 330 μM/h while Reg_ was unrestricted. In our optimized fits, Reg_ was ~50% open under both conditions ([Fe_C] in the first and second rows of Table 1 was ~30 μM, which equals K_C). Likewise, the rates of import of Fe into the mitochondria and vacuoles remained unchanged (k_M and k_V were the same in the first and second rows). In contrast, the cell-growth rate (given by α in Table 1) in the late exponential stage of YPAD cells was approximately half of what it was in early exponential growth.

Fe import rates were better synchronized to cell growth as cells moved from late exponential phase to slow-growth stage. Specifically, the growth rate and the rates of import of Fe into the cell all declined 10-fold, as did the rates of import of Fe into vacuoles and mitochondria (compare simulation data in the second and third rows of Table 1).

Connection to Known Regulatory Systems. Our results show that the high-affinity Fe uptake system (as monitored by

Fet3p expression) was functioning during exponential growth, even with an Fe^{III} citrate concentration of 40 μM in the medium. A previous study found that Fet3p was not expressed in cells grown on the same medium and harvested early in the transition period.[23] This is slightly different from what our model predicts (namely that the high-affinity system should still be active at this stage), but it would be consistent with our model if the cells used for the Fet3p Western blot had actually been harvested slightly later, in the stationary state.

The low-affinity system may involve Fet4p, a divalent metal transporter on the plasma membrane, and/or Smf1. Because Fet4p is still active when cells are grown with 1 mM Fe-containing medium,[32] Fet4p appears to be responsible for the uptake of Fe in cells grown on high-Fe concentration media; under these conditions, cells express almost no Fet3p.[23] The variation of Fet4p expression with changes in growth mode needs to be evaluated, but we suspect that Fet4p is the major Fe importer during post-exponential growth.

High-Blocking Temperature Nanoparticles. We report here a second type of nanoparticle in WT cells grown under post-exponential conditions. These nanoparticles differ in terms of magnetic and probably structural and compositional properties from those formed in the mitochondria of ISC mutant strains. Although we do not understand these differences well, our results suggest a difference in the blocking temperature (T_B).[27] ISC mutant-associated nanoparticles exhibit a quadrupole doublet at 5 K, suggesting T_B < 5 K, whereas the second type of nanoparticle appears to be magnetic at 5 K, suggesting T_B > 5 K. Beyond that, the broad and unresolved MB and EPR signatures associated with the "high-blocking temperature" (HBT) nanoparticles make further characterization difficult, nor do we know their location in WT cells. A small proportion of nanoparticles appears to be present in mitochondria (as evidenced in MB spectra of isolated WT mitochondria), but the amount was small relative to the overall concentration of nanoparticles present in these cells. The quantity present was far smaller than the amount that accumulates in mitochondria in ISC mutant strains. The majority of nanoparticles that formed in post-exponentially grown WT cells were nonmitochondrial.

Two locations for HBT nanoparticles seem likely, namely, vacuoles and the cytosol, but at this point, we cannot distinguish between them. Nishida et al. identified nanoparticles in vacuoles,[33] and we have found that the Fe in vacuoles is indeed susceptible to the formation of nanoparticles (of the low-blocking temperature type).[10] The source of this susceptibility is uncertain, but Fe^{III} polyphosphate (which is closely related to vacuolar Fe) forms nanoparticles at high pH (e.g., 7). The vacuolar lumen is acidic, with pH values between 4.5 and 5.5 being typical.

A recent report indicates that aging and mitochondrial dysfunction are associated with an increase in vacuolar pH.[34] Post-exponential cells are old, raising the intriguing possibility that decreased acidity in vacuoles causes mononuclear HS Fe^{III} species in vacuoles to precipitate as nanoparticles. Losing a proton from a coordinated water could help generate a bridge between two mononuclear complexes. This process, occurring repeatedly throughout a population of HS Fe^{III} complexes, could cause nanoparticles to form. Because nanoparticles are precipitated aggregates, this process would be sensed by the cell as a decline in the level of vacuolar Fe (despite the fact that Fe is accumulating), prompting additional Fe_C to be imported from the cytosol into the organelle.

Lack of Correlation between Iron Accumulation and ROS Damage. Iron is generally considered to be deleterious to the cell when in excess, because it can catalyze the formation of hydroxyl radicals and other ROS.[1] Indeed, we and others have linked ROS damage in mitochondria to nanoparticle formation in that organelle.[17,28,35] In the study presented here, we found no correlation between ROS formation and Fe accumulation. Vacuoles have an enormous capacity to store Fe; perhaps the sequestration of Fe into vacuoles prevents ROS from being generated. The same may not hold true for mitochondria. These organelles in WT cells appear to be more strictly regulated in terms of Fe, such that massive quantities of nanoparticles do not normally accumulate in them. Nanoparticles generated in other nonmitochondrial compartments may not significantly damage the cell, suggesting that in a nonmitochondrial context, nanoparticles are more of a nuisance than a danger. Another consideration is that in slow-growing or stationary-state cells, Fe-associated ROS may have been eliminated (by the ROS response machinery of the cell) faster than it was generated.

Insights from the Model. Although simple, the chemically based mathematical model captures essential behavior of global Fe metabolism in *S. cerevisiae* cells. The model illustrates the balance of processes that determines the concentrations of the four major groups of Fe in the cell, namely, cytosolic, mitochondrial, vacuolar, and nanoparticulate. These processes include high- and low-affinity import pathways, import into two organelles, conversion into nanoparticles, and the growth rate of the cell. The model predicted the distribution of the four major groups of Fe as observed by MB. The quantitative effects obtained by simulation can be rationalized qualitatively from the chemical model depicted in Figure 8, viewing the growth rate as an increase in cell volume that dilutes all cellular species.

Two versions of the model were considered, including one that assumed that nanoparticles form from cytosolic Fe_C (version C) and one that assumed that they form from vacuolar Fe_V (version V). Simulations using version C fit the data 22% better than those generated using version V, which suggests that nanoparticles form in the cytosol. However, we do not regard this as sufficient grounds to eliminate version V. There is no independent evidence that nanoparticles can form in the cytosol, whereas nanoparticles have been observed in isolated vacuoles.[10] Further studies are required to settle this issue.

R_{LO} contributed 30 μM/h of Fe import under both exponential and post-exponential growth conditions. The low-affinity Fe import system was unregulated with respect to stages of cell growth. In contrast, the high-affinity system R_{HI} was regulated (our model could not reproduce the data without including such regulation). The molecular-level details of this regulation are not well understood, so we employed a surrogate Reg_ function to mimic the effect. Under YPAD and MM exponential conditions, R_{HI} imported Fe at a rate of ~150 μM/h $\{(330 \times 1)/[1 + (32/30)^3]\}$, corresponding to ~80% of total Fe influx. During slow-growth or stationary phases, simulations indicated that R_{HI} imported Fe at a rate of ~24 μM/h $\{(330 \times 1)/[1 + (70/30)^3]\}$, representing ~40% of the total Fe influx.

The unusual situation that led to an unregulated condition occurred in the late-exponential/transition period. Here, $[Fe_C]$ was approximately the same as it was during the exponential phase (i.e., the valve was ~50% open) even though cells were growing half as fast (and thus cellular component concentrations were being diluted half as fast). This caused the unregulated influx of Fe. [Fe_C] did not increase, as would have otherwise occurred, because a substantial portion converted, either directly or indirectly, into nanoparticles. These particles are not sensed by the cell yet suppress the increase in [Fe_C] that would otherwise shut down Fe import. Thus, Fe continued to flow into the cell at the exponential-growth-mode level. This is the cause of unregulated Fe homeostasis in post-exponential yeast cells.

Previous Studies and the Importance of Growth Rate. In our previous studies, cells grown in medium containing ferric citrate concentrations as high as 10 mM did not show cellular Fe concentrations that were as high as those observed here.[23] Why? In those studies, cells were harvested in the late exponential phase (OD of 1.2), perhaps before the Fe accumulation phenomenon became severe. Our current study reveals that the mode of growth near the time of harvesting is critically important in dictating the extent of Fe accumulation.

This study illustrates the importance of growth rate in understanding Fe import, trafficking, and regulation. Unfortunately, the time dependence of regulation has not been emphasized in previous studies of cellular Fe metabolism. In many published studies involving the Fe metabolism of yeast, the exact growth mode and growth rate at the time of harvesting are not even mentioned. We show here that such information will be important for accurately interpreting the phenotype of various Fe-associated mutant strains. The excess Fe that accumulates in yeast cells during post-exponential growth periods could confuse such interpretations and obscure the primary function of the mutated protein, a typical objective of such studies. In the future, those studying Fe metabolism in yeast should ideally focus on the Fe content of *exponentially* growing cells to provide insight into Fe-related metabolism and the primary function of associated proteins. During exponential growth, nanoparticle formation is minimal such that regulatory effects will not be distorted.

Is the Lack of Iron Regulation in Cells Unique? Virtually all cellular reactions are enzyme-catalyzed and thus are genetically (and/or allosterically) regulated by the cell. Importantly, enzyme-catalyzed reactions are generally orders of magnitude faster than noncatalyzed reactions. Because of this, noncatalyzed reactions are generally irrelevant from the cell's perspective; the cell is living in a faster time domain. Iron evades cellular control because nanoparticles can form rapidly via nonenzymatically catalyzed reactions, at rates that depend on very general chemical properties of the cell such as pH and redox status. The cell has no means of sensing this formation apart from the indirect (and distorting) effect that it has on cytosolic Fe concentrations. Thus, in the case of Fe, the cell simply tolerates a bit of chaos. Fortunately, such nanoparticle-forming reactions are not lethal as they do not generate toxic levels of ROS. Although we cannot state unequivocally that this lack of cellular regulation is unique for Fe, we are unaware of other cellular metabolites that are unregulated. Such an occurrence for another cellular component would seem to require a similar combination of reaction chemistry that we regard as highly unlikely.

■ ASSOCIATED CONTENT

Ⓢ Supporting Information

Fet3p expression levels in cells harvested at different time points (Figure S1), chronological profile of Zn concentrations in cells for 5 days (Figure S2), 100 K MB spectrum of cells grown in MM for 5 days (Figure S3), MB spectrum of mitochondria isolated from cells grown in MM for 5 days (Figure S4), loading controls for Western blots (Figure S5), ODEs for version V (Figure S6), and Mössbauer parameters determined from the spectra in the main text (Table S1). This material is available free of charge via the Internet at http://pubs.acs.org.

■ AUTHOR INFORMATION

Corresponding Author

*E-mail: Lindahl@chem.tamu.edu. Phone: (979) 845-0956. Fax: (979) 845-4719.

Funding

This study was funded by the National Institutes of Health (GM084266), the National Science Foundation (DMS-0714896), and the Robert A. Welch Foundation (A1170).

Notes

The authors declare no competing financial interest.

■ ACKNOWLEDGMENTS

We thank Andrew Dancis (University of Pennsylvania, Philadelphia, PA) for providing the DY150 strain and the Fet3p antibody, Valeria Culotta (Johns Hopkins University, Baltimore, MD) for providing the Sod2p antibody, and Brad Pierce (University of Texas, Arlington, TX) for allowing us to use his EPR spectrometer.

■ ABBREVIATIONS

CD, central doublet; DNP, 2,4-dinitrophenyl; DT, doubling time; EPR, electron paramagnetic resonance; HI, high-affinity pathway; HBT, high blocking temperature; HS, high-spin; ICP-MS, inductively coupled plasma mass spectrometry; ISC, iron/sulfur cluster; LO, low-affinity pathway; LS, low-spin; MB, Mössbauer; MM, minimal medium; NHHS, nonheme high-spin; OD, optical density; ODE, ordinary differential equation; ROS, reactive oxygen species; YPAD, yeast extract, peptone, adenine hemisulfate, and dextrose; WT, wild type.

■ REFERENCES

(1) Imlay, J. A. (2003) Pathways of oxidative damage. *Annu. Rev. Microbiol. 57*, 395−418.

(2) Van Ho, A., Ward, D. M., and Kaplan, J. (2002) Transition metal transport in yeast. *Annu. Rev. Microbiol. 56*, 237−261.

(3) Lill, R., and Müehlenhoff, U. (2008) Maturation of iron-sulfur proteins in eukaryotes: Mechanisms, connected processes, and diseases. *Annu. Rev. Biochem. 77*, 669−700.

(4) Stearman, R., Yuan, D. S., Yamaguchi-Iwai, Y., Klausner, R. D., and Dancis, A. (1996) A permease-oxidase complex involved in high-affinity iron uptake in yeast. *Science 271*, 1552−1557.

(5) Shakoury-Elizeh, M., Tiedeman, J., Rashford, J., Ferea, T., Demeter, J., Garcia, E., Rolfes, R., Brown, P. O., Botstein, D., and Philpott, C. C. (2004) Transcriptional remodeling in response to iron deprivation in *Saccharomyces cerevisiae*. *Mol. Biol. Cell 15*, 1233−1243.

(6) Dix, D. R., Bridgham, J. T., Broderius, M. A., Byersdorfer, C. A., and Eide, D. J. (1994) The FET4 gene encodes the low-affinity Fe(II) transport protein of *Saccharomyces cerevisiae*. *J. Biol. Chem. 269*, 26092−26099.

(7) Waters, B. M., and Eide, D. J. (2002) Combinatorial control of yeast FET4 gene expression by iron, zinc, and oxygen. *J. Biol. Chem. 277*, 33749−33757.

(8) Cyert, M. S., and Philpott, C. C. (2013) Regulation of cation balance in *Saccharomyces cerevisiae*. *Genetics 193*, 677−713.

(9) Froschauer, E. M., Schweyen, R. J., and Wiesenberger, G. (2009) The yeast mitochondrial carrier proteins Mrs3p/Mrs4p mediate iron

transport across the inner mitochondrial membrane. *Biochim. Biophys. Acta 1788*, 1044−1050.

(10) Cockrell, A. L., Holmes-Hampton, G. P., McCormick, S. P., Chakrabarti, M., and Lindahl, P. A. (2011) Mössbauer and EPR study of iron in vacuoles from fermenting *Saccharomyces cerevisiae*. *Biochemistry 50*, 10275−10283.

(11) Li, L. T., Chen, O. S., Ward, D. M., and Kaplan, J. (2001) CCC1 is a transporter that mediates vacuolar iron storage in yeast. *J. Biol. Chem. 276*, 29515−29519.

(12) Li, L., Bagley, D., Ward, D. A., and Kaplan, J. (2008) Yap5 is an iron-responsive transcriptional activator that regulates vacuolar iron storage in yeast. *Mol. Cell. Biol. 28*, 1326−1337.

(13) Puig, S., Askeland, E., and Thiele, D. J. (2005) Coordinated remodeling of cellular metabolism during iron deficiency through targeted mRNA degradation. *Cell 120*, 99−110.

(14) Kosman, D. J. (2003) Molecular mechanisms of iron uptake in fungi. *Mol. Microbiol. 47*, 1185−1197.

(15) Reverter-Branchat, G., Cabiscol, E., Tamarit, J., and Ros, J. (2004) Oxidative damage to specific proteins in replicative and chronological-aged *Saccharomyces cerevisiae*: Common targets and prevention by calorie restriction. *J. Biol. Chem. 279*, 31983−31989.

(16) Felice, M. R., De Domenico, I., Li, L. T., Ward, D. M., Bartok, B., Musci, G., and Kaplan, J. (2005) Post-transcriptional regulation of the yeast high affinity iron transport system. *J. Biol. Chem. 280*, 22181−22190.

(17) Miao, R., Kim, H., Koppolu, U. M. K., Ellis, E. A., Scott, R. A., and Lindahl, P. A. (2009) Biophysical characterization of the iron in mitochondria from Atm1p-depleted *Saccharomyces cerevisiae*. *Biochemistry 48*, 9556−9568.

(18) Lindahl, P. A., Morales, J. G., Miao, R., and Holmes-Hampton, G. (2009) Isolation of *Saccharomyces cerevisiae* mitochondria for Mössbauer, EPR, and electronic absorption spectroscopic analyses. In *Methods in Enzymology, Vol 456: Mitochondrial Function, Part A: Mitochondrial Electron Transport Complexes and Reactive Oxygen Species* (Allison, W. S., Ed.) pp 267−285, Elsevier, Amsterdam.

(19) Miao, R., Holmes-Hampton, G. P., and Lindahl, P. A. (2011) Biophysical investigation of the iron in Aft1-1(up) and Gal-YAH1 *Saccharomyces cerevisiae*. *Biochemistry 50*, 2660−2671.

(20) Kitagaki, H., Cowart, L. A., Matmati, N., Montefusco, D., Gandy, J., de Avalos, S. V., Novgorodo, S. A., Zheng, J., Obeid, L. M., and Hannun, Y. A. (2009) ISC1-dependent metabolic adaptation reveals an indispensable role for mitochondria in induction of nuclear genes during the diauxic shift in *Saccharomyces cerevisiae*. *J. Biol. Chem. 284*, 10818−10830.

(21) Singh, A., Severance, S., Kaur, N., Wiltsie, W., and Kosman, D. J. (2006) Assembly, activation, and trafficking of the Fet3p·Ftr1p high affinity iron permease complex in *Saccharomyces cerevisiae*. *J. Biol. Chem. 281*, 13355−13364.

(22) Yoon, H., Klinzing, G., and Blanch, H. W. (1977) Competition for mixed substrates by microbial-populations. *Biotechnol. Bioeng. 19*, 1193−1210.

(23) Holmes-Hampton, G. P., Jhurry, N. D., McCormick, S. P., and Lindahl, P. A. (2013) Iron content of *Saccharomyces cerevisiae* cells grown under iron-deficient and iron-overload conditions. *Biochemistry 52*, 105−114.

(24) Palmiter, R. D., and Huang, L. P. (2004) Efflux and compartmentalization of zinc by members of the SLC30 family of solute carriers. *Pfluegers Arch. 447*, 744−751.

(25) Holmes-Hampton, G. P., Miao, R., Morales, J. G., Guo, Y. S., Münck, E., and Lindahl, P. A. (2010) A nonheme high-spin ferrous pool in mitochondria isolated from fermenting *Saccharomyces cerevisiae*. *Biochemistry 49*, 4227−4234.

(26) Park, J., McCormick, S. P., Chakrabarti, M., and Lindahl, P. A. (2013) Insights into the iron-ome and manganese-ome of Δ*mtm1* *Saccharomyces cerevisiae* mitochondria. *Metallomics 5*, 656−672.

(27) Papaefthymiou, G. C. (2010) The Mössbauer and magnetic properties of ferritin cores. *Biochim. Biophys. Acta 1800*, 886−897.

(28) Miao, R., Martinho, M., Morales, J. G., Kim, H., Ellis, E. A., Lill, R., Hendrich, M. P., Münck, E., and Lindahl, P. A. (2008) EPR and Mössbauer spectroscopy of intact mitochondria isolated from Yah1p-depleted *Saccharomyces cerevisiae*. *Biochemistry 47*, 9888−9899.

(29) Lesuisse, E., Santos, R., Matzanke, B. F., Knight, S. A. B., Camadro, J.-M., and Dancis, A. (2003) Iron use for haeme synthesis is under control of the yeast frataxin homologue (Yfh1). *Hum. Mol. Genet. 12*, 879−889.

(30) Flattery-O'Brien, J. A., Grant, C. M., and Dawes, I. W. (1997) Stationary-phase regulation of the *Saccharomyces cerevisiae* SOD2 gene is dependent on additive effects of HAP2/3/4/5- and STRE-binding elements. *Mol. Microbiol. 23*, 303−312.

(31) Jhurry, N. D., Chakrabarti, M., McCormick, S. P., Gohil, V. M., and Lindahl, P. A. (2013) Mössbauer study and modeling of iron import and trafficking in human Jurkat cells. *Biochemistry. 52*, 7926−7942.

(32) Dix, D., Bridgham, J., Broderius, M., and Eide, D. (1997) Characterization of the FET4 protein of yeast: Evidence for a direct role in the transport of iron. *J. Biol. Chem. 272*, 11770−11777.

(33) Nishida, K., and Silver, P. A. (2012) Induction of biogenic magnetization and redox control by a component of the target of rapamycin complex 1 signaling pathway. *PLoS Biol. 10*, e1001269.

(34) Hughes, A. L., and Gottschling, D. E. (2012) An early age increase in vacuolar pH limits mitochondrial function and lifespan in yeast. *Nature 492*, 261−265.

(35) Bulteau, A.-L., Dancis, A., Gareil, M., Montagne, J.-J., Camadro, J.-M., and Lesuisse, E. (2007) Oxidative stress and protease dysfunction in the yeast model of Friedreich ataxia. *Free Radical Biol. Med. 42*, 1561−1570.